Journal of Remote Sensing
A SCIENCE PARTNER JOURNAL

REVIEW

Recipes for the Derivation of Water Quality Parameters Using the High-Spatial-Resolution Data from Sensors on Board Sentinel-2A, Sentinel-2B, Landsat-5, Landsat-7, Landsat-8, and Landsat-9 Satellites

Juliana Tavora[1*], Binbin Jiang[2], Thomas Kiffney[3], Guillaume Bourdin[3], Patrick Clifton Gray[4], Lino Sander de Carvalho[5], Gabriel Hesketh[6], Kristin M. Schild[7,8], Luiz Faria de Souza[5], Damian C. Brady[3], and Emmanuel Boss[3]

[1]Faculty of Geo-Information Science and Earth Observation (ITC), University of Twente, PO Box 217, 7500 AE Enschede, The Netherlands. [2]State Key Laboratory of Marine Geology, Tongji University, Shanghai, China. [3]School of Marine Sciences, University of Maine, Orono, ME, USA. [4]Nicholas School of the Environment, Duke University Marine Lab, Beaufort, NC, USA. [5]Departamento de Meteorologia, Universidade Federal do Rio de Janeiro, Rio de Janeiro, Brazil. [6]Department of Marine Sciences, University of Southern Mississippi, Ocean Spring, MS, USA. [7]School of Earth and Climate Sciences, University of Maine, Orono, ME, USA. [8]Climate Change Institute, University of Maine, Orono, ME, USA.

*Address correspondence to: j.tavora@utwente.nl

Citation: Tavora J, Jiang B, Kiffney T, Bourdin G, Gray PC, de Carvalho LS, Hesketh G, Schild KM, de Souza LF, Brady DC, et al., Recipes for the Derivation of Water Quality Parameters Using the High-Spatial-Resolution Data from Sensors on Board Sentinel-2A, Sentinel-2B, Landsat-5, Landsat-7, Landsat-8, and Landsat-9 Satellites. *J. Remote Sens.* 2023;3:Article 0049. https://doi.org/10.34133/remotesensing.0049

Submitted 21 December 2022
Accepted 16 May 2023
Published 5 June 2023

Satellites have provided high-resolution (<100 m) water color (i.e., remote sensing reflectance) and thermal emission imagery of aquatic environments since the early 1980s; however, global operational water quality products based on these data are not readily available (e.g., temperature, chlorophyll-*a*, turbidity, and suspended particle matter). Currently, because of the postprocessing required, only users with expressive experience can exploit these data, limiting their utility. Here, we provide paths (recipes) for the nonspecialist to access and derive water quality products, along with examples of applications, from sensors on board Landsat-5, Landsat-7, Landsat-8, Landsat-9, Sentinel-2A, and Sentinel-2B. We emphasize that the only assured metric for success in product derivation and the assigning of uncertainties to them is via validation with in situ data. We hope that this contribution will motivate nonspecialists to use publicly available high-resolution satellite data to study new processes and monitor a variety of novel environments that have received little attention to date.

Introduction

In the past 30 years, a series of papers have shown the utility of high-spatial-resolution remote sensing to study coastal and inland water using sensors on board the Landsat series of satellites, in particular, looking at the distribution of suspended particulate matter (SPM) and chlorophyll-*a* (Chl-*a*) [1–6]. Deriving such data is not trivial as the top-of-the-atmosphere (TOA) signal in the visible bands is overwhelmed by the impact of the atmosphere, and, thus, all these studies had to perform an atmospheric correction (AC) step. However, such data, as well as those from the recently launched Sentinel-2 satellites, are extremely useful for water quality monitoring by providing unparalleled spatial scale (on the order of 10 s of meters) of utility to aquaculturists [7,8], recreational users, and water quality managers [9–11].

At present, however, such data are still not widely distributed (in contrast to data from lower resolution satellites, further offshore) and require specialized training for their derivation. In addition, since the Landsat series of satellite has been collecting consistent color and thermal data since the mid-80s (Landsat-5, Landsat-7, Landsat-8, and Landsat-9)—these data could be exploited to study, for example, the impact of land use, decadal oscillations, and climate change on long time series using water quality in rivers, lakes, and coastal locations spanning a period of almost 40 years. Satellite water color sensors measure the radiance (L_t) at the TOA. This radiance results from the additive contributions (Eq. 1) of radiance emanating from within the water, radiance interacting with the water surface, and radiance that is (multiply) scattered by atmospheric gases and aerosols (Table 1) [12].

Table 1. Notation of symbols and acronyms.

Symbol	Description	Unit
L_t	Total radiance at the TOA	$W{\cdot}m^{-2}{\cdot}sr^{-1}{\cdot}nm^{-1}$
L_R	TOA radiance due to molecular scattering in the atmosphere	$W{\cdot}m^{-2}{\cdot}sr^{-1}{\cdot}nm^{-1}$
L_a	TOA radiance due to scattering by aerosols only	$W{\cdot}m^{-2}{\cdot}sr^{-1}{\cdot}nm^{-1}$
L_{aR}	TOA radiance due to aerosol-molecule scattering	$W{\cdot}m^{-2}{\cdot}sr^{-1}{\cdot}nm^{-1}$
L_g^{TOA}	TOA radiance due to sun glint	$W{\cdot}m^{-2}{\cdot}sr^{-1}{\cdot}nm^{-1}$
L_{sky}^{TOA}	TOA radiance due to surface-reflected background sky	$W{\cdot}m^{-2}{\cdot}sr^{-1}{\cdot}nm^{-1}$
L_{wc}^{TOA}	TOA radiance due to whitecaps and foam	$W{\cdot}m^{-2}{\cdot}sr^{-1}{\cdot}nm^{-1}$
L_w	TOA radiance emanating from within the water	$W{\cdot}m^{-2}{\cdot}sr^{-1}{\cdot}nm^{-1}$
ρ_w	Water-leaving reflectance, $\rho_w = R_{rs}{\cdot}\pi$	—
E_d	Downwelling irradiance	$W{\cdot}m^{-2}{\cdot}sr^{-1}{\cdot}nm^{-1}$
θ_v	Viewing direction	Degree
θ_s	Solar zenith angle	Degree
ϕ	Azimuthal angle measured relative to the Sun's azimuthal direction	Degree
$0^+, 0^-$	above, and below water surface	—
λ	Wavelength (i.e., satellite band)	nm
R_{rs}	Remote sensing reflectance (water color)	sr^{-1}
$\delta_{Rrs}(\lambda)$	$R_{rs}(\lambda)$ uncertainty	sr^{-1}

$$L_t = L_R + \left[L_a + L_{aR}\right] + L_g^{\mathrm{TOA}} + L_{sky}^{\mathrm{TOA}} + L_{wc}^{\mathrm{TOA}} + L_w^{\mathrm{TOA}} \quad (1)$$

An important parameter for derivation of water quality, satellite water leaving reflectance, ρ_w (Eq. 2), is derived from the processing of the measured L_t to obtain the water-leaving radiance (L_w) in a process called AC [12].

$$\rho_w(\theta_v, \phi) = \pi \frac{L_w(\theta_v, \phi, O^+)}{E_d(\theta_s, O^+)} = \pi R_{rs}(\theta_v, \phi, O^+) \quad (2)$$

Remote sensing reflectance, R_{rs}, is the ratio of the water leaving radiance at the water surface (L_w) to the downwelling irradiance (E_d). R_{rs} is a function of the inherent optical properties (IOPs; namely, backscattering and absorption). The IOPs are functions determined of the concentration and composition of water quality parameters such as Chl-*a*, SPM, and colored dissolved organic matter (CDOM) [13]. These water quality parameters are what is retrieved by "inverting", that is applying algorithms to R_{rs} or ρ_w to obtain water quality parameters. To make R_{rs} as independent as possible from sun zenith and satellite viewing angles, a "normalization" procedure is often performed (see the Normalization during reflectance derivation section and [12]).

For readers new to the fields of aquatic optics and aquatic remote sensing, we suggest Mobley's book as an introduction (https://ioccg.org/wp-content/uploads/2022/01/mobley-oceanicopticsbook.pdf). In addition, the International Ocean Colour Coordinating Group report series (https://ioccg.org/what-we-do/ioccg-publications/ioccg-reports/) contains a wealth of information and definitions of the terminology that you will find along the document.

Our goal in this work is to present recipes for nonspecialists to derive water quality data using publicly available data and open-source tools. We emphasize that the only way to assess the quality of data obtained and their associated uncertainties is through validation with in situ data. Similar validation has to be conducted for operational products from low-spatial-resolution satellites in inland waters and coastal areas as assumptions true to the open ocean may not be valid nearshore (e.g., covariation of dissolved organics and Chl-*a*, a simplified marine atmosphere for AC). Note that even in open ocean environments, water quality products may be biased as they have been developed with limited datasets [14]. While we focus on the coastal ocean, our recipes are applicable to freshwater lakes and rivers as well, with minor modification (e.g., adjusting for elevation in the AC step for Alpine lakes). Throughout this document, we adopt the term "water color" to denote the remotely sensed reflectance, R_{rs}; however, it is also referred to as "ocean color", "ocean color remote sensing", and "aquatic color" in the literature.

High-resolution remote sensing of aquatic environments is a very active area of research, and novel approaches and analytical tools are added often. We encourage readers to stay abreast of innovations that may be pertinent for their specific needs. We note that since 2020, provisional products using Sentinel-2 have been generated by the European Space Agency (ESA) for coastal Europe and a few other locations at 100-m resolution (https://resources.marine.copernicus.eu/products) and that provisional data using Landsat-8 and Landsat-9 are available from US Geological Survey (USGS) upon request (see the Provisional aquatic reflectance from USGS: Coastal to Gulf Stream R_{rs} and Chl-*a* section).

Materials and Methods

The main ingredient for deriving water color data is the level 1C data, which is georeferenced and calibrated data at the TOA.

While surface reflectance data (level 2) are provided for the Landsat and Sentinel-2 visible bands, their quality may not be sufficient to derive most water quality products [15], as the AC applied has not been designed for a dark target such as water. Surface temperature data are also available at level 2 and have become recently available in collection 2 for the Landsat satellite series (although a linear calibration equation is necessary to convert to temperature; see Eq. 3) and are of sufficient quality to be directly useful (e.g., [16]). We will therefore separate the recipes (Fig. 1) for water temperature from those derived from water color (i.e., SPM, turbidity, and Chl-*a*). The latter parameters necessitate an AC step to derive level 2 (water surface) data from level 1 TOA data.

The decision of which data products to use will depend on the specific application. Each satellite sensor (and hence derived products) has different spatial, spectral, and temporal resolutions as well as radiometric sensitivity. Along with the revisit period of the satellite, the spatial resolution (i.e., the pixel size) of a satellite image is one of the essential aspects of remote sensing, as it determines the level of detail captured. Although it is intuitive to assume that a higher spatial resolution is always desirable, in reality, the choice of level of detail depends both on the application needs and on computational capacity available. Figure 2 exemplifies the visual impact of different spatial resolutions on surface coastal water features.

Because of their small footprint compared to traditional ocean observing satellites, high-resolution satellite sensors (pixel size < 100 m) usually have a long revisit period (see Table S1) in comparison to near daily coverage by their low-spatial-resolution counterparts (e.g., Moderate Resolution Imaging Spectroradiometer (MODIS)-aqua or Sentinel 3-OLCI). Temporal resolution increases as one approaches the poles due to the convergence of longitudes and as one combines data from several satellites operating on different schedules. Overpass times for specific satellites are available using, for example, a tool provided by NASA (https://oceandata.sci.gsfc.nasa.gov/overpass_pred/).

Landsat and Sentinel-2 missions have different spectral and radiometric resolutions, i.e., bandwidths, center wavelengths, signal-to-noise ratio, and number of bands. Landsat-5 and Landsat-7 particularly have relatively low signal-to-noise ratio and spectral resolutions, which makes it challenging to retrieve water quality products with high fidelity. USGS provides a summary of Landsat known issues (https://www.usgs.gov/landsat-missions/landsat-known-issues). These limitations, however, are not meant to discourage the reader from carrying out analysis using either Landsat-5 or Landsat-7 but to raise awareness and provide proper interpretation of results. Landsat-8, Landsat-9, Sentinel-2A, and Sentinel-2B, on the other hand, have higher spectral and radiometric resolutions. Tables S2 and S3 summarize their characteristics.

Recipe for water color products (SPM and Chl-*a*)

Obtaining level 1C data

The source of level 1C data depends on the satellite sensor of choice: Landsat-5, Landsat-7, Landsat-8, and Landsat-9 (for all sensors mentioned in Table S1) data are available from USGS (https://earthexplorer.usgs.gov), while Sentinel-2A and Sentinel-2B

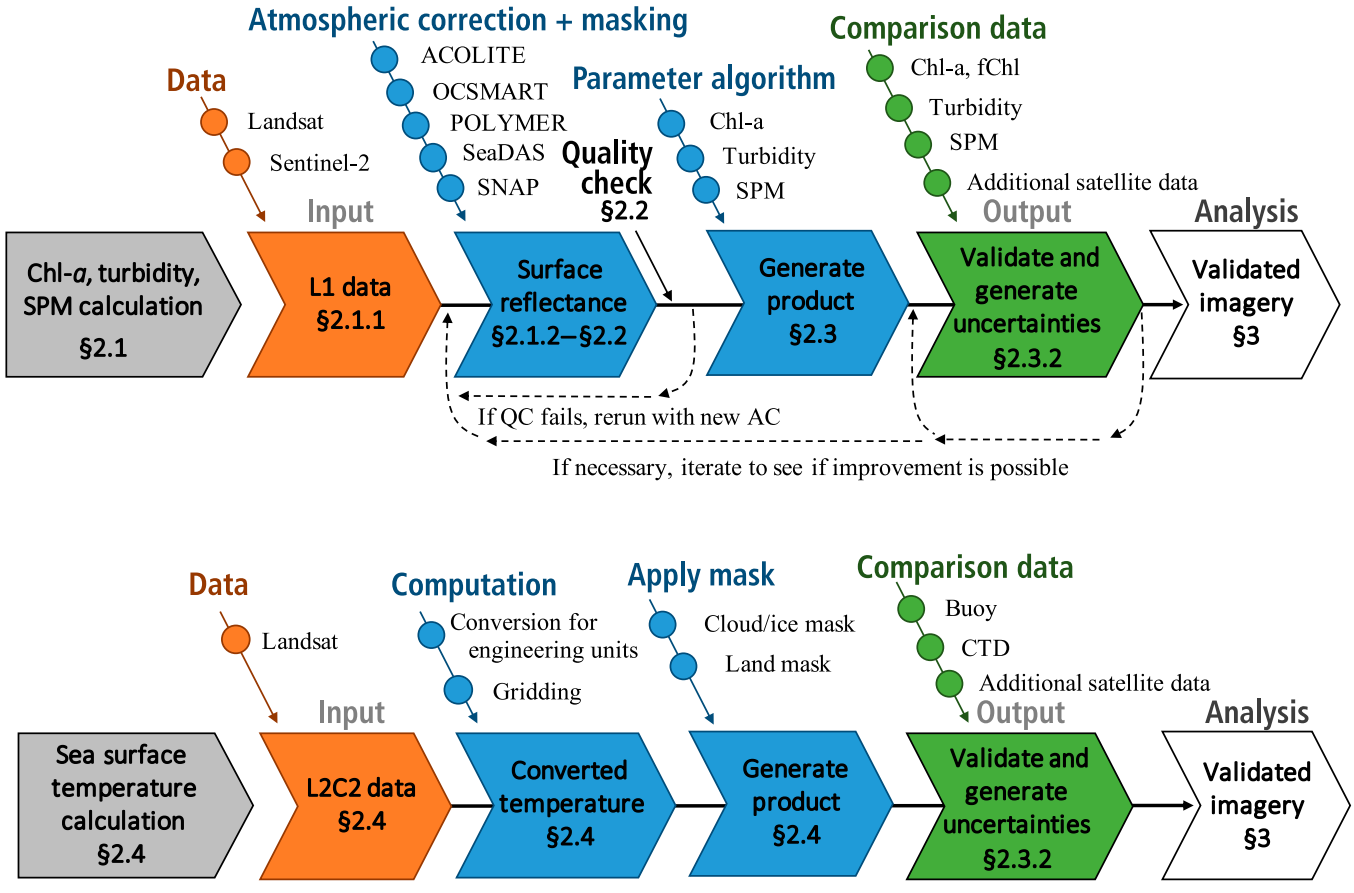

Fig. 1. Schematic of the recipe elements to obtain satellite-derived water quality products.

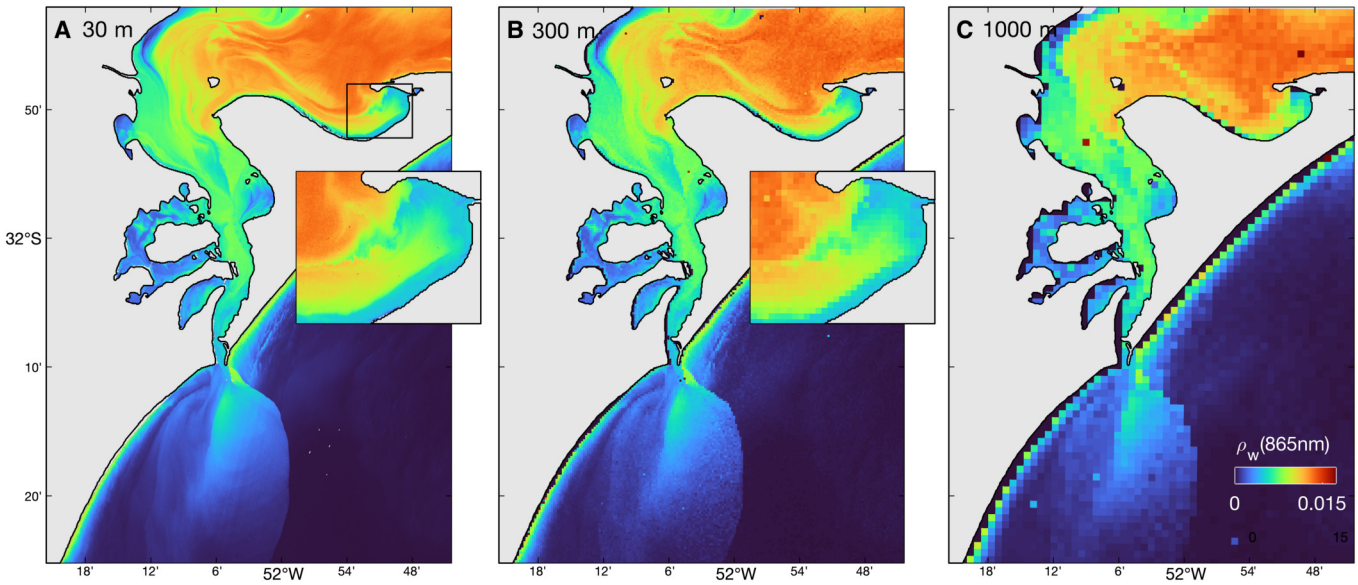

Fig. 2. Comparison of different spatial resolutions simulated from a Landsat-8 scene for a pixel size of 30 m (original Landsat-8 scene) (A), 300 m (B) and 1,000 m (C). (A) and (B) have each a zoomed subset depicting differences in pixel size when one deals with smaller areas, while (C) shows clear differences already in large areas. Landsat-8 scene was re-sampled using SNAP software. Note that small inland features such as reservoirs or lakes are also affected by the spatial resolution of the satellite sensor.

data are available from ESA (https://scihub.copernicus.eu/) web platforms. Historical data from Sentinel-2A and Sentinel-2B (e.g., on Copernicus, older than 12 months) may not be available for direct download, requiring an order beforehand. ESA also distributes their products through several platforms via the Data and Information Access Services (https://www.copernicus.eu/en/access-data/dias), each offering different spatial and temporal resolutions. While satellite data can be obtained for a given scene at the web portals above, we developed a single Python-based tool [getOC (https://github.com/OceanOptics/getOC)] to batch download NASA and ESA satellite data (for both low- and high-resolution sensors) and simplify data acquisition. Detailed instructions can be found in the GitHub link above. This tool automatically queries different data platforms and downloads all available images for the selected dates and locations. It uses 2 different data platforms, each maintained either by NASA or by ESA, hence requiring a registration to EarthData (https://urs.earthdata.nasa.gov/users/new) for NASA satellites and CreoDIAS (https://portal.creodias.eu/register.php) for ESA satellites. Support for USGS EarthExplorer to download Landsat scenes will be implemented soon.

AC for water color data

Once the level 1C data are acquired, AC procedures are necessary. ACs remove the effects of atmospheric gases and aerosols from the satellite scene (which often contributes >90% of the signal at the TOA) as well as accounts for whitecaps and glint (for reviews, see [12,17,18] for NASA's AC approach). There are many AC schemes available in the public domain (e.g., Table 2). These AC schemes are based on a range of methods and provide a choice of options to derive R_{rs} or ρ_w [19], from which water quality parameters (i.e., products) are derived. Some of these software have a graphical user interface (GUI) and tools to merge images in time and space (e.g., SeaDAS, SNAP, and ACOLITE), while others do not (e.g., POLYMER). These tools also differ in their capacity to derive water quality products (e.g., ACOLITE), although this step could be applied independently. Here, we introduce 5 software environments that implement an AC (multiple options exist in some software environments; Table 2): ACOLITE, OCSMART, POLYMER, SeaDAS, and SNAP, as well as examples using each of them. For further information about comparative performance of different ACs, refer to [19–22]. Note that (a) the majority of the AC software (i.e., OCSMART, POLYMER, and SNAP) does not perform AC on Landsat-5 and Landsat-7, which can represent an obstacle for long time series; and (b) because of the large atmospheric contribution to the measured TOA radiance, different AC schemes, as well as different algorithms to derive products from above water reflectance, will likely result in characteristically different estimates of water quality products [23]. Therefore, quality assurance (QA) and quality control (QC) steps must be applied to R_{rs} and the derived products (see below) to ensure that the AC was successful.

- ACOLITE: Developed at the Royal Belgium Institute of Natural Sciences, ACOLITE has a detailed user manual and forum, both of which provide instruction and full support, especially useful for new users. The software is available in GUI and command line (CLI) modes and is available as Python source code (GitHub or https://odnature.naturalsciences.be/remsem/software-and-data/acolite). ACOLITE batch processing is only available in CLI mode, for which steps are described and setup is available (https://odnature.naturalsciences.be/remsem/acolite-forum/viewtopic.php?t=29). It provides 2 AC schemes: dark spectrum fitting (hereafter DSF) [24] and exponential extrapolation (hereafter Exp) [25,26]. The Exp scheme uses Rayleigh-corrected reflectance to estimate aerosol reflectance in 2 short wave infrared (SWIR) bands (i.e., infrared by default) and extrapolates to the near-infrared (NIR) visible bands. However, a possible flaw in SWIR exponential extrapolation when considering adjacency effects and sun glint may lead to overestimation

Table 2. AC schemes by software.

AC	Option	Software	Satellite	Run time[a]	Difficulty level[b]
DSF	Dark spectrum	ACOLITE	L5, L7, L8, L9, S2A, S2B	10 min 23 s	II
Exp	Exponential	ACOLITE	L5, L7, L8, L9, S2A, S2B	4 min 48 s	II
OCSMART	Machine learning	OCSMART	L8, L9[c], S2A, S2B	5 min 55 s (60 m)	I
POLYMER	Function of glint, aerosol	POLYMER	L8, S2A, S2B	23 min 34 s	IV
l2gen	2	SeaDAS	L5, L7, L8, L9, S2A, S2B	2 h 33 min	V
C2RCC	C2RCC-Nets	SNAP	L8, S2A, S2B	18 min 54 s	III
C2X	C2X-Nets	SNAP	L8, S2A, S2B	18 min 13 s	III

Run time is based on processing a Sentinel-2 scene (20-m resolution) in middle of Gulf of Maine from 2021.06.18 on high-performance computer with a Linux OS (refer to Fig. 5D for a visual of the scene).

[b]Difficulty level are represented from I (easiest) to V (hardest) determined on the basis of the effort needed to apply them by the same user (B.J.) based on batch processing Sentinel-2 scene with Linux OS.

[c]According to contact with the software developer, OCSMART, and POLYMER plan to support Landsat-9. C2RCC is not yet fully adapted for Landsat-9 (https://forum.step.esa.int/t/problems-encountered-in-processing-landsat8-9-images-with-c2rcc/36806).

of ρ_w for which case the Exp becomes inadequate. The DSF scheme uses multiple dark targets to avoid overestimation by the Exp approach in ACOLITE.

- OCSMART: Ocean Color—Simultaneous Marine and Aerosol Retrieval Tool (OCSMART) is a multisensor data analysis platform designed to retrieve aerosol and water color products from satellite remote sensing images. OCSMART uses multilayer neural networks trained using an extensive set of radiative transfer simulations based on a coupled atmosphere–ocean radiative transfer model to perform the AC and subsequent retrieval of ocean IOPs [27]. The software (http://www.rtatmocn.com/oc-smart/) runs on UNIX and Windows.
- POLYMER: Developed by F. Steinmetz, P.-Y. Deschamps, and D. Ramon [28] and maintained and distributed by HYGEOS (https://forum.hygeos.com/viewforum.php?f=5), POLYMER comes with a detailed README file and a forum. The software is available via the CLI only. POLYMER models the spectral reflectance of the atmosphere, sun glint, and water using a polynomial fit on all visible bands. This separation of the contribution from different sources allows a relatively accurate recovery of water reflectance even where other AC schemes based only on NIR bands fail due to high glint contamination.
- SeaDAS: Developed and maintained by NASA, SeaDAS is a software package for processing, displaying, analyzing, and quality-controlling remote sensing data (download at https://seadas.gsfc.nasa.gov). The software runs on the UNIX and Windows OS but can be used in a Windows OS with additional steps (https://seadas.gsfc.nasa.gov/client_server/). SeaDAS currently provides several AC schemes via its l2gen processor (see Table S1) that are applied on a pixel-by-pixel basis. The Earthdata forum provides excellent support for debugging with SeaDAS (https://forum.earthdata.nasa.gov/viewforum.php?f=7&sid=7b8a85eb704352689d10b1e972f22870).
- SNAP: Developed and maintained by ESA, the Sentinel Application Platform (SNAP) is a software package for processing, displaying, analyzing, and quality-controlling remote sensing data (download at https://step.esa.int/main/download/snap-download/). The software runs on the UNIX and Windows OS. Embedded in SNAP is the Case 2 Regional CoastColour (C2RCC) model that performs an AC intended for coastal waters using a neural network algorithm ([29]).

To carry out any AC, we require ancillary data in addition to level 1C data (e.g., surface pressure, winds, ozone concentration, etc.). ACOLITE, OCSMART, POLYMER, and SeaDAS automatically download the latest version of ancillary data available for each scene from Earthdata (https://urs.earthdata.nasa.gov). In POLYMER, the user may instead choose the European Centre for Medium-Range Weather Forecasts Reanalysis dataset for the ancillary data. SNAP, however, requires that the user downloads the ancillary data, which can be found at the water color data repository (https://oceandata.sci.gsfc.nasa.gov/directaccess/Ancillary/). It is important to note that ancillary data are not available in real time, and there may be several weeks between the time of acquisition and when the scene analyzed. If near real-time products are needed, an educated guess at the value of the ancillary data (e.g., based on a local climatology) may be used but may bias the derived output.

Normalization during reflectance derivation

While R_{rs} is intended to be a product of the IOPs of the water (i.e., absorption and scattering), R_{rs} is an apparent optical property because it is affected by other factors such as the geometry of sun and satellite. To minimize the impact of viewing geometry, we apply the normalization schemes. These convert the measured R_{rs} to a normalized reflectance with the sun at zenith and account for the satellite viewing angle and some atmospheric effect [12,30,31]. A very detailed account of this normalization is provided in Section 3 of book [12]. It is important to realize

that not all AC schemes introduced above (e.g., ACOLITE) compute a normalized reflectance and hence may result in a different value for a water quality parameter when using algorithms, which assume that the reflectance is normalized. For Landsat data, POLYMER computes normalized reflectance, requiring the angle band files created using the USGS's L8 Angle tool (https://www.usgs.gov/landsat-missions/solar-illumination-and-sensor-viewing-angle-coefficient-files).

Georeferencing and data grids

While it may be expected that remote sensing data are available in even grids of latitudes and longitudes, this is not the case. A variety of reasons stemming from satellite orbits and distances between longitude lines changing with latitude explain this non-regularity. Therefore, it is critical to map the data onto a grid for analysis and plotting and to test that this transformation is done correctly. The assignment of geographic coordinates for each data point is addressed at level 1C. To ensure that level 2 data are mapped correctly to a grid, specific functions are available in geographical information system (GIS) software and in computing environments such as Python and MATLAB (e.g., the MATLAB function "geotiffinfo.m" can be used to extract the latitude and longitude coordinate of each point; see codes in the Supplementary Materials). A good test to determine whether your program correctly maps the data is to add the location of moorings with validation data into your scene and confirm that the buoy location is where you expect it (e.g., when compared to Global Positioning System coordinates or Google Earth).

Masking and QC

Masks

Almost every remote sensing scene contains areas where R_{rs} cannot be accurately retrieved because of clouds, cloud shadows, glint, land, vegetation shadow, ice, or shallow areas where bottom reflectance affects the water leaving radiance. Masking these pixels is crucial to avoid biased or unrealistic data. Examples of existing coastal waters masking criteria for the software tools we mentioned above, especially those focusing on clouds, are in Table 3. However, there are invariably cases when existing masks do not cover what users may conclude are erroneous or biased results. In such cases, users could and should devise their own criterion (e.g., reflectance threshold above or below a specific value, areas where reflectance does not pass a QA/QC criterion) and document these customized criteria when sharing results with others.

Adjacency effect

Atmospheric scattering of light can result in the contamination of light measured at a specific location by light from nearby areas. If the adjacent areas are substantially different in their reflectance (e.g., snow-covered land near a dark coastal ocean), the darker water pixels may be materially affected. Adjacency effects can cause issues for distances up to about 40 km from the coastline [32]. Contamination from adjacency effects can be diagnosed by looking for and avoiding regions with expressive spatial gradients in reflectance at relevant wavelengths in the direction from the coast toward the water (e.g., [21,33,34]). The POLYMER AC can recover relatively good data quality even when it is affected by adjacency effects; moreover, the vegetation adjacency correction was added in version 4.15 [28,35].

Stripping

Image artifacts, particularly stripping, affect image quality and the quality of water color products estimated from remote sensing data. Stripping is an image artifact in the along or across-track direction that results from different factors, such as sensor characteristics, poor calibration, and imaging processing itself. In aquatic environments, stripping is notably problematic since the low radiance values from water targets can be of similar magnitude as the variability imposed by the artifacts. The medium- to low-resolution sensors commonly used for water color studies [e.g., Visible Infrared Imaging Radiometer Suite (VIIRS), and Sea-viewing Wide Field-of-view Sensor (SeaWIFS), and MODIS] have long had stripping issues [36,37]; however, high-resolution sensors, particularly sensors within the Landsat program and Sentinel constellation, exhibit similar stripping issues when applied to water color [15,38,39]. Noise patterns in Sentinel-2 images have been reported to be highly variable, which can lead to a misinterpretation of water color since features observed can be attributed to either image striping patterns or the variability of ocean optical properties [40]. On the other hand, previous studies using Sentinel-2 imagery have shown that stripping did not affect the retrieving of water IOPs, and authors argue that the error introduced by stripping is not sufficiently high to affect the IOP signal [41]. Destripping methods have long been applied to remote sensing sensors [42]. MODIS and VIIRS have been the focus for most of the testing in destripping methods with expressive improvement in image stripping issues [36,43,44]. Although stripping filters have been applied for Landsat and Sentinel-2 program sensors [45,46], when dealing with water color, fewer studies have shown promising results [40].

Table 3. Masking schemes for clouds and shadows.

AC software	Type of artifact	Methods	Source
ACOLITE	Cloud	$\rho_{surf}(1{,}609) > 0.0215$	[19]
OCSMART	Cloud	$\rho_{rc}(865) > 0.027$; $\varepsilon < 2.5$	[27]
POLYMER	Cloud	$\rho_{surf}(865) > 0.2$	[19]
SeaDAS	Cloud	Coastal waters: $\rho_{surf}(1{,}609) > 0.018$; open ocean: $\rho_{surf}(865) > 0.027$	[19]
SNAP	Cloud	IdePix	[19]
	Thin cloud, shadows	WiPE algorithm	[69]

QC of the reflectance spectra

Reflectance spectra, while highly variable between different environments, are constrained in the spectral shapes that they exhibit. A tool based on a library of high-quality spectra has been created to assess the likelihood that a reflectance spectra is reasonable [47], assigning a quality score that can be used to filter nonphysical spectra and suggest which AC works best in a given environment. The tool is available for Sentinel-2 and Landsat-8 (https://oceanoptics.umb.edu/score_metric/) for which a score between 0 and 1 is assigned to the targeted spectrum, with 1 for likely good R_{rs} spectra and 0 for likely unusable R_{rs} spectra. Since this scoring system's publication, an additional tool has been created called the Quality Water Index Polynomial (QWIP) [48]. The QWIP is based on the Apparent Visible Wavelength (AVW) [49], a one-dimensional geophysical metric of color that is inherently correlated to spectral shape calculated as a weighted harmonic mean across visible wavelengths. QWIP is computed on the basis of a polynomial relationship between the hyperspectral AVW and a Normalized Difference Index using red and green wavelengths. The QWIP value represents the difference between a spectrum's AVW and Normalized Difference Index and the QWIP polynomial. A QWIP score of less than −0.2 or greater than 0.2 for a spectrum indicates that it is likely a bad spectrum [48].

Derivation of water quality products

Once R_{rs} or water leaving reflectance ($\rho_w = \pi \times R_{rs}$) has been obtained and quality-controlled, water quality parameters can be derived. Algorithms to obtain water quality products from R_{rs} are available in the literature or can be empirically derived by the user based on relationships obtained with their own dataset. Algorithms are either explicit (i.e., based on an equation that relates R_{rs} at a given band or ratios of bands to a water quality product) or implicit (i.e., generated using a neural network or other machine learning technique). Explicit algorithms can be purely statistical or can incorporate some knowledge of radiative transfer (referred to as semianalytic). Robust algorithms are most often the ones that a user did not tune to their own data. On the other hand, it could be that local conditions are sufficiently different from other environments that only a locally tuned algorithm provides unbiased products (e.g., local sediment mineralogy effect on suspended SPM retrieval). For instance, implicit band ratio-based algorithms can potentially minimize the sensitivity to effects of particle size and density.

To obtain SPM, algorithms typically use red and NIR wavelengths where water typically dominates absorption. Since water absorption is often dominating in the red and NIR wavelengths, R_{rs} is proportional to backscattering by particles (i.e., particle concentration). The relationship between R_{rs} and backscattering (or SPM, or turbidity) is linear at low concentrations, but as concentration increases, particle contribution to absorption increases changing the sensitivity of R_{rs} to SPM, a process called saturation [50]. Since water absorption is generally monotonically increasing in the red and NIR, shifting to longer wavelengths as SPM concentration increases [51] or using a multiwavelengths algorithm [52] helps to increase the sensitivity of R_{rs} to SPM. Table 4 provides a summary of different types of SPM and turbidity algorithms.

Algorithms for extracting biological information from ocean color (e.g., Chl-*a* and CDOM) are making large advances but are still in development. Typical empirical Chl-*a* algorithms designed for the open ocean are not likely to work well in many coastal environment where assumptions of water constituents covarying in the open ocean may break down in coastal environments. Thus, locally tuned algorithms are likely to be more successful. A summary of different types of Chl-*a* algorithms

Table 4. Types of SPM and turbidity algorithms.

	Algorithm type	Reference example	Satellite sensor
Explicit	Band ratio	[70]	L8, L9, S2A, S2B
	Semianalytical single band	[57,59][a]	L5, L7, L8, L9, S2A, S2B
	Semianalytical band switch	[51,71]	L8, L9, S2A, S2B
	Semianalytical multiple bands	[52]	L5, L7, L8, L9, S2A, S2B
Implicit	Radiative transfer	[72][b]	S2A, S2B
	Machine learning	[53]	L8, L9, S2A, S2B

[a]The algorithm setup allows for application to high-resolution sensors. We suggest that coefficients be adapted (see the Spectral convolution section).

[b]Adapted for Sentinel 2/MSI by Arabi et al. [73].

Table 5. Types of Chl-*a* algorithms.

	Algorithm type	Reference example	Satellite sensor
Explicit	Band ratio	[74]	L8, L9
Implicit	Radiative transfer	[72][a]	S2A, S2B
	Machine learning	[53]	L8, L9, S2A, S2B

[a] [72] Adapted for Sentinel 2/MSI by Arabi et al. [73]

is provided in Table 5. Algorithms have been developed to obtain colored dissolved organic material absorption (CDOM) from Landsat, Sentinel-2A, and Sentinel-2B; however, their uncertainty is large because of their strong sensitivity to AC, and we thus elected not to emphasize them here. Interested readers are referred to [53,54].

Spectral convolution

In instances of converting from hyperspectral resolution to specific multispectral bands (e.g., to compare reflectance computed with in situ hyperspectral sensors to that obtained from a satellite), convolution of the hyperspectral data and the spectral response function (SRF) of the multispectral band of interest will need to be undertaken. Spectral convolution is possible for a range of satellite parameters or derived water quality products including IOPs (e.g., [55]). Note that SRF should be applied to radiances rather than to reflectance when computing lower resolution R_{rs} [56]. SRF are available online for Sentinel-2 (https://sentinels.copernicus.eu/web/sentinel/user-guides/sentinel-2-msi/document-library/-/asset_publisher/Wk0TKajiISaR/content/sentinel-2a-spectral-responses) and for Landsat (https://landsat.usgs.gov/spectral-characteristics-viewer). Spectral convolution is often necessary when combining time series from sensors with different spectral characteristics, to validate instruments (e.g., compare in situ R_{rs} with airborne R_{rs} [57] or space-borne R_{rs} [58]) and to apply retrieval algorithms calibrated to specific sensors. However, spectral convolution is commonly a forgotten step in the process of deriving water quality products, potentially introducing biases [55,56].

In the case of applying algorithms for water quality products, a few bio-optical algorithms apply a spectral convolution within the calculation [52], while other widely applied semianalytical algorithms such as the work of Nechad et al. [59] for turbidity or Nechad et al. [57] for SPM provide hyperspectral coefficients calculated for narrow bandwidth sensors (typically <10 nm) that need to be transformed to match spectral characteristics of broader band sensors (such as the ones onboard Landsat-5 to Landsat-9 or Sentinel-2). For these satellite sensors, Vanhellemont [24] provides turbidity coefficients calculated from [59,60] and Tavora et al. [66] provides SPM coefficients calculated from the original coefficients available in [57].

Assigning uncertainties to derived products

Traditionally, uncertainty estimates are obtained from an analysis comparing in situ measured data to data derived from water color and temperature. A variety of statistical metrics are computed to assess how well the product compares to in situ data. The most commonly applied statistical methods include a simple linear regression with significance level of at least 5% (i.e., $\alpha \leq 0.05$). A linear regression typically retrieves at least 2 values: the linear correlation coefficient (r) and its associated p-value. The r value will define the strength of the linear relationship between in situ and estimated/modeled data, while the value represents the probability that the linear correlation occurred by chance. Note that often the logarithm of an ocean product is compared to the logarithm of the product derived from R_{rs}, as both are typically log-normally distributed [61]. The linear correlation coefficient, however, is not enough to assess the uncertainties, as it is strongly dependent on the dynamic range of the data and is not useful in obtaining an uncertainty (either absolute or relative). Therefore, parameters such as root mean square error, mean absolute percentage error, bias, and others are often calculated (e.g., Table 1 in [62]). Note that, most often, both the product from remote sensing and the validation data have significant uncertainties. In such cases, it is best to use type-II regressions, which are regressions that account for uncertainties in both independent and dependent variables [63]. A useful package that estimates point by point uncertainties when regressing 2 variables is available from MBARI (https://www.mbari.org/introduction-to-model-i-and-model-ii-linear-regressions/). Doing so ensures that points with larger uncertainties are weighted less in the regression than those with less uncertainty. While the goodness of fit will be lower for the line obtained in a weighed regression compared to a regression that does not take uncertainties into account, the weighed regression obtained is more robust and very likely more accurate.

More complete assessments of uncertainties may include uncertainties from both in situ data and remote-sensing-derived products. For in situ methods, uncertainties can be derived from equipment calibration in the case of turbidimeters and weight triplicates in the case of gravimetric methods. For remote-sensing-derived products, uncertainties may include AC, intrinsic assumptions in the algorithm of choice to derive SPM and the range of $R_{rs}(\lambda)$ values within a sampling box (for a comprehensive treatment, see [64]). Uncertainties may also come from the inherent mismatch between methods of data acquisition regardless of equipment calibration, algorithm accuracy, or AC. The in situ data used are of several types: either at fixed point (e.g., moorings, or water samples) or from moving platforms (e.g., ships) collecting samples at variable water

Table 6. Overview of case studies.

Satellite-derived product	Site	Satellite name and sensor	Case study section
SST	Coast of Maine, USA	L8/TIRS	Maine Coast SST
SPM	Svalbard, NOR	L8/OLI	Tempelfjorden, Svalbard SPM
Turbidity	Patos Lagoon, BRA	L5/TM, L7/ETM+, L8/OLI, L9/OLI	Long-term turbidity estimates from Patos Lagoon Estuary, Brazil
Chl-*a*	Coast of Maine, USA	S2A, S2B /MSI	Coastal Maine Chl-*a*
$R_{rs}(\lambda)$ and Chl-*a*	Gulf Stream, USA	L8/OLI, L9/OLI	Provisional aquatic reflectance from USGS: Coastal to Gulf Stream 476 R_{rs} and Chl-*a*

depths and promoting local turbulence (i.e., affecting shallow waters to a higher degree while effect may be minimal over deeper waters). In general, water samples collected at depth ranging between 0 and 1 m are considered as surface samples. Satellite sensors, on the other hand, capture data integrated in space (i.e., within the pixel size) and averaged for a window of pixels (typically ranging between 3 and 7 pixels [64]). In addition satellite scenes capture information over different depths for each band, with that depth being dependent on water clarity. This inherent difference between the spatial scale of the in situ samples used as reference for validation and the satellite scales implies an inherent uncertainty; that is, we expect that differences could be large for any given match-up and hence the need to obtain as many match-ups as possible (so as to discern if bias exist). Finally, uncertainties tend to be proportional to the magnitude of the measurement at moderate to large values (due to the nature of the algorithm's uncertainties), while at low values, absolute uncertainties tend to dominate (e.g., due to instrument resolution).

Another way to evaluate the success of derived water quality and water color product is to compare the distribution of properties in time and/or space [64,65], rather than regress

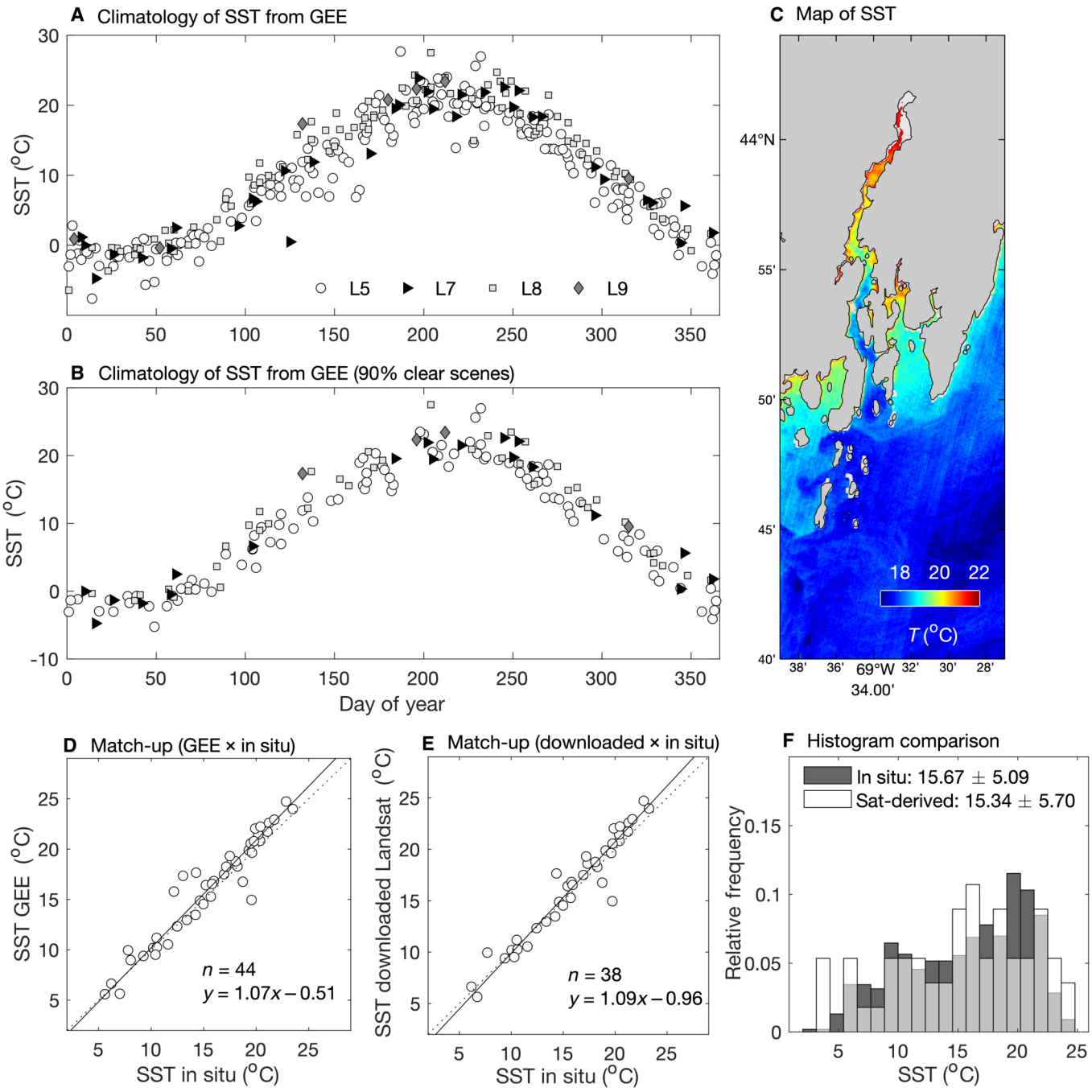

Fig. 3. Climatology of SST along the coast of Maine, USA estimated from GEE (A and B) at different cloud coverages. Points with a standard deviation greater than 10 °C were removed ($n = 1$). (C) depicts spatial variability of SST from a downloaded L8/TIRS scene from 2022 September 14. (D) represents the relationship between the in situ SST and SST from GEE, and (E) shows the relationship between in situ SST and Landsat-derived SST (downloaded scenes). (F) is a comparison between SST extracted from Landsat (GEE-derived) and in situ SST.

individually matched values. For example, a potential comparison could be of the frequency distribution of SPM measured at a mooring location over a year to all the remotely retrieved values that the mooring represents. This allows for more data to be involved in the comparison than those available from strict match-ups. If the 2 distributions overlap well, confidence is gained in the inversion. If one is biased compared to the other, it could indicate that the specific algorithm or AC used creates a biased product. Before concluding that the fault is in the procedure generating the products, careful consideration should be made that no bias in sampling (space/time) could cause the observed bias (e.g., including too many near-coast points that are typically associated with larger values in SPM).

- Chl-*a*: The most reliable way to validate Chl-*a* is with in situ water samples filtered onto a filter, frozen before analysis, and analyzed using high-performance liquid chromatography. Unfortunately, collecting and analyzing such samples is time-consuming and expensive and requires trained personnel. Less expensive analyses include in vitro fluorescence and spectrophotometry. Autonomous methods for Chl-*a* are also possible (e.g., in vivo fluorescence or spectrophotometry) allowing for high-frequency sampling but requiring that a proxy relation be derived using higher accuracy methods.
- SPM and turbidity: Also regularly called total suspended matter (TSM) or suspended sediment concentration (SSC), SPM is estimated in situ by either (a) using side- or backscattering sensors that often are calibrated to provide turbidity units [66] or (b) collecting water samples for which gravimetric analysis has been carried out, allowing conversion to SPM through a proxy relation. The 2 methods can be used in tandem to provide cross calibration for the scattering sensor(s). Best practices on water sampling and validation of turbidity and SPM are summarized in [67].
- Temperature: Also regularly called SST (sea surface temperature), temperature is commonly measured in situ using conductivity, temperature, and depth instruments or less commonly simple temperature probes.

For additional details regarding methods to collect these samples, see the Ocean Best Practices repository (https://www.oceanbestpractices.org/).

Recipe for temperature

There is currently only one source of high-resolution temperature data, the Landsat satellite series. It can be accessed either by (a) direct download through the USGS website or (b) through Google Earth Engine (GEE). Both platforms provide the most recent collection 2 level 2 data. Unlike the recipe for color data, level 2 surface temperature provided from the Landsat series does not require additional AC, although it should always be validated against in situ data in a new region.

To directly download the temperature data, we access collection 2 level 2 data from USGS Earth Explorer site (https://earthexplorer.usgs.gov/). Useful step-by-step streaming videos are accessible under key words "download Landsat", for example. USGS provides a tool to make bulk downloads of Landsat-8 and Landsat-9 data (https://dds.cr.usgs.gov/bulk). With satellite data in hand, the user can continue processing through GUI-based GIS tools (e.g., QGIS and ArcGIS) or coding platforms (e.g., MATLAB and Python). Instead of downloading and working with data locally, temperature data can also be accessed through GEE. GEE hosts a large number of freely available remote sensing datasets and enables users to analyze large amounts of remote sensing data without downloading scenes to their computer [68], which is particularly attractive for long time-series analyses. The GEE online code editor allows users to perform similar analyses as in a GIS or MATLAB, visualize, and download results [68]. For temperature estimates using

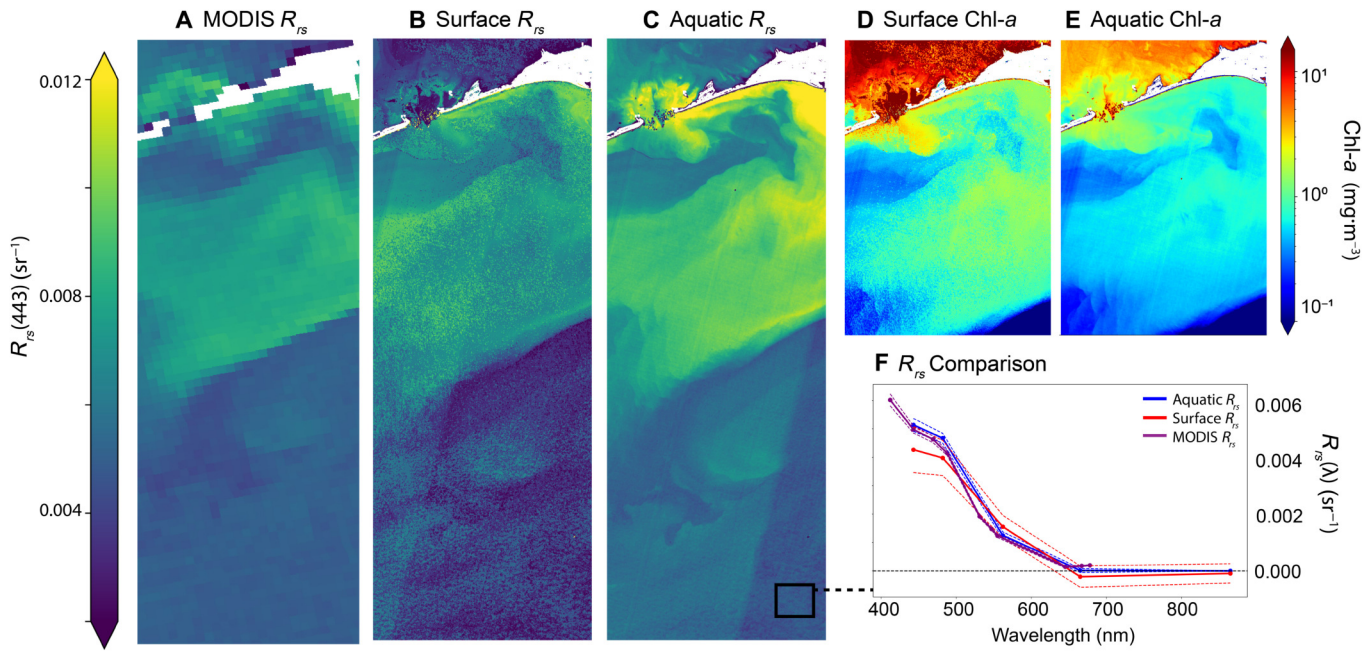

Fig. 4. Comparison of MODIS-Aqua R_{rs} (A), with standard Landsat R_{rs} (B), and Landsat-9 Aquatic R_{rs} (C) centered at 443 nm. (D) and (E) show Chl-*a* calculated using the OC3 algorithm tuned to Landsat wavelengths. (F) shows the mean R_{rs} spectra from each method for the patch of the Gulf Stream outlined in the black rectangle [in (C)] and highlights both the lower blue reflectance from the standard Landsat product and its much higher variation. All imagery is projected in UTM Zone 18N.

either GEE or a coding platform, the Landsat-8 and Landsat-9 thermal band used is band 10 (10.6 to 11.19 µm) which is provided as an unsigned integer (band 11 for Landsat-8 suffers from stray light and is not discussed here). To convert it to temperature in both GEE and coding platforms, we use the following equation:

$$\text{Temperature} = \text{Band}_{10} * 0.00341802 + 149 - 273.15 \ (^{\circ}\text{C}) \quad (3)$$

While a land mask is available from collection one, we have found that using a threshold on band 7 (shortwave infrared, 2.11 to 2.29 µm) provides a simple delineation of the higher reflective land ($\text{Band}_{7,\text{cal}} > 0.15$, where Band_7 was converted to engineering units $\text{Band}_{7,\text{cal}} = \text{Band}_7 * 0.0000275 - 0.2$). The conversion factors were obtained from USGS documentation (https://www.usgs.gov/core-science-systems/nli/landsat/landsat-collection-2-level-2-science-products). The pixel-by-pixel uncertainties in the temperature is given in the "...ST QA.TIF" file as an unsigned integer and should be multiplied by 0.01 (table 6-1 in https://d9-wret.s3.us-west-2.amazonaws.com/assets/palladium/production/s3fs-public/media/files/LSDS-1619_Landsat-8-9-C2-L2-ScienceProductGuide-v4.pdf.

Note that the temperature obtained is that of a layer shallower than 1 mm of the surface water, not representing the full water column. Hence, it should not be surprising if a bias of around 1 to 2 °C is found during the day relative to a sensor 1 m below surface in the summer at a highly stratified estuary under calm conditions.

Case Studies

In this section, we share a few examples where we applied the recipes described above (see Table 6) to showcase the concepts and issues described above. These are examples of high-resolution satellite products derived for a variety of water bodies (Fig. S1) using different ACs and processing workflows. We share all the associated codes (see information in the Supplementary Materials) and data so that users have an opportunity to practice before working with their own data. We use the term surface reflectance for USGS level 2 atmospherically corrected reflectance designed for land application. We discourage its use for the derivation of water quality parameters but include it here in 2 case studies to contrast it with derived water R_{rs}.

Maine Coast SST

Here, we demonstrate retrieving coastal SST from the Damariscotta River estuary, a narrow estuary in Maine, USA, where traditional 1-km by 1-km SST products cannot accurately represent the region. We showcase the steps for directly downloading from the USGS in the Recipe for temperature section and processing the scene in MATLAB and GEE. To follow along with the direct download method, the user will need to retrieve a level 2 SST image from USGS (link in the Masking and QC section). To use the same region and image as the example code, we select path 11, row 30 under the search criteria, and download the product bundle for 14 July 2013. In addition to the scene, we will need the function *getLandsatL2 SST* from GitHub (https://github.com/OceanOptics/getLandsatL2_SST). This function extracts the SST information and automatically applies Eq. 3 from the Recipe for temperature section. The example MATLAB script in the Supplementary Materials contains code using "getLandsatL2 SST.m" function and will plot a downloaded image and extract data for a site of interest. While directly downloading and working with scenes are needed for certain analyses, it can be a labor intensive process. For example, the user would have to download all available images in

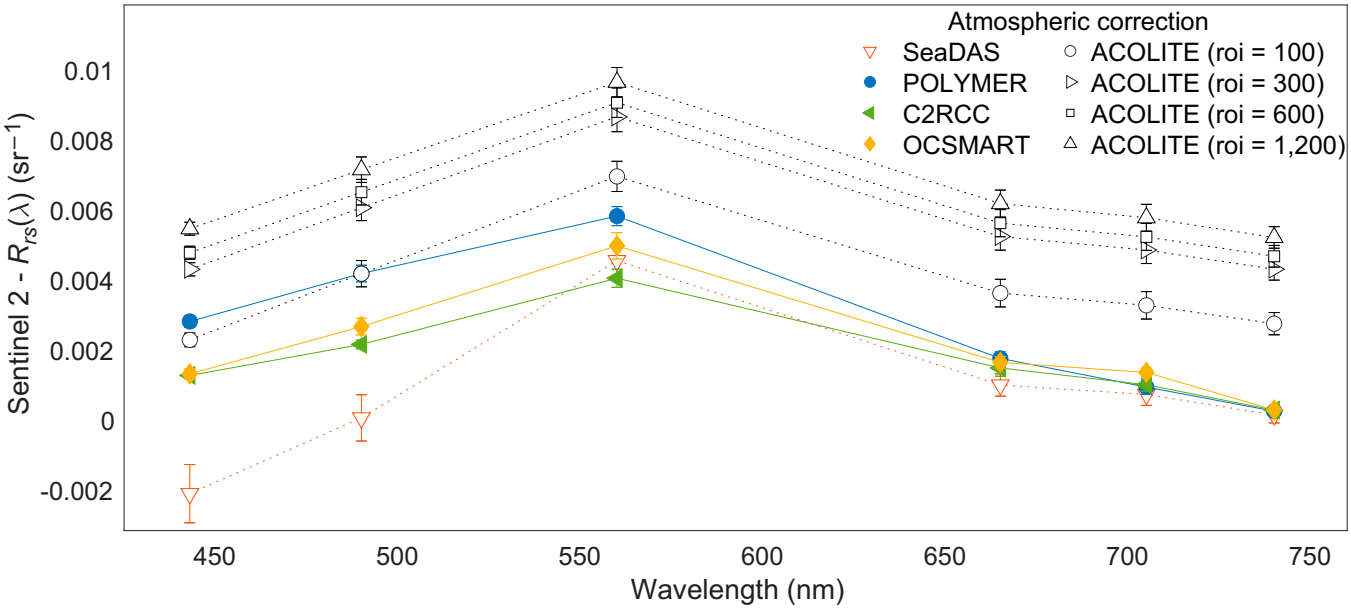

Fig. 5. $R_{rs}(\lambda)$ for a Sentinel-2 (20-m resolution; of 2018 May 18) scene at the Upper Damariscotta River, USA. The same satellite scene was processed using ACOLITE's AC on 4 different regions of interest (roi; 100-by-100-, 300-by-300-, 600-by-600- and 1,200-by-1,200 pixels), as well as C2RCC, SeaDAS, OCSMART, and POLYMER ACs. Note that we do not expect negative R_{rs} values (by definition it is ≥0) and, at low turbidity as observed in this location, we expect near zero values of reflectance in the NIR wavelengths. C2RCC, POLYMER, and OCSMART are consistent with expectations for this image. White-filled symbols represent spectral profiles failing the QWIP algorithm test (i.e., ACOLITE and SeaDAS). QWIP scores are 6.10 (SeaDAS), 0.15 (POLYMER), 0.18 (C2RCC), 0.16 (OCSMART), 0.22 (ACOLITE roi = 100), 0.31 (ACOLITE roi = 300), 0.33(ACOLITE roi = 600), and 0.34 (ACOLITE roi = 1,200).

their region and loop through each image to generate a climatology as in Fig. 3A and B.

Our GEE example (see Fig. 3) explores the Landsat series available within the "Landsat Collections" GEE dataset. Although Landsat collection 2 contains level 1 data from Landsat-1 to Landsat-9, it also contains science products for sensors within Landsat-4 to Landsat-9. The biggest advantage of using GEE is the possibility of compiling a time series of different Landsat collection 2 products rapidly and without downloading the data locally. The example GEE script in the Supplementary Materials contains code to compile collection 2 Landsat SST products for Landsat-5, Landsat-7, Landsat-8, and Landsat-9 thermal infrared sensors (TIRSs). The script masks both land and cloud cover based on the Normalized Difference Water Index and Landsat's QA_PIXEL and QA_RADSAT bands (https://www.usgs.gov/landsat-missions/landsat-collection-2-quality-assessment-bands), respectively. It also merges all 3 sensors, applying 3 different resampling schemes (i.e., one pixel, 3×3, and 5×5 window box). It generates a time series for one specific path and row, here specifically for the Damariscotta River estuary, including all images available for that area with a limiting cloud percentage of 90%.

Provisional aquatic reflectance from USGS: Coastal to Gulf Stream R_{rs} and Chl-*a*

If Landsat-8 and Landsat-9 are appropriate for your study area and research goal, there is a relatively simple option to obtain high-quality satellite imagery suitable for water color analysis. The USGS provides, upon request, a provisional "aquatic reflectance" product generated from the Level 1 Landsat-8 and Landsat-9 data. These data are available globally from March 2013 onward, and requests simply require submitting the scene ID (e.g., LC09 L1TP 014035 20211109 20220119 02 T1) to the USGS processing interface (https://espa.cr.usgs.gov/). These scenes can be ordered individually or in bulk.

The USGS combines the initial Landsat level 1 data along with auxiliary atmospheric data (atmospheric pressure, water vapor, aerosol, wind, etc.) to atmospherically correct the data (using l2gen in SeaDAS as outlined in [6]). These water leaving radiances are normalized by the downwelling irradiance to retrieve R_{rs}. In a final step, the retrieved R_{rs} is multiplied by π to obtain the aquatic reflectance ρ_w. While the product is still provisional and as of this publication has yet to be validated globally and across all water types, it has been assessed and found to be a high-quality source of water color data with a stable AC.

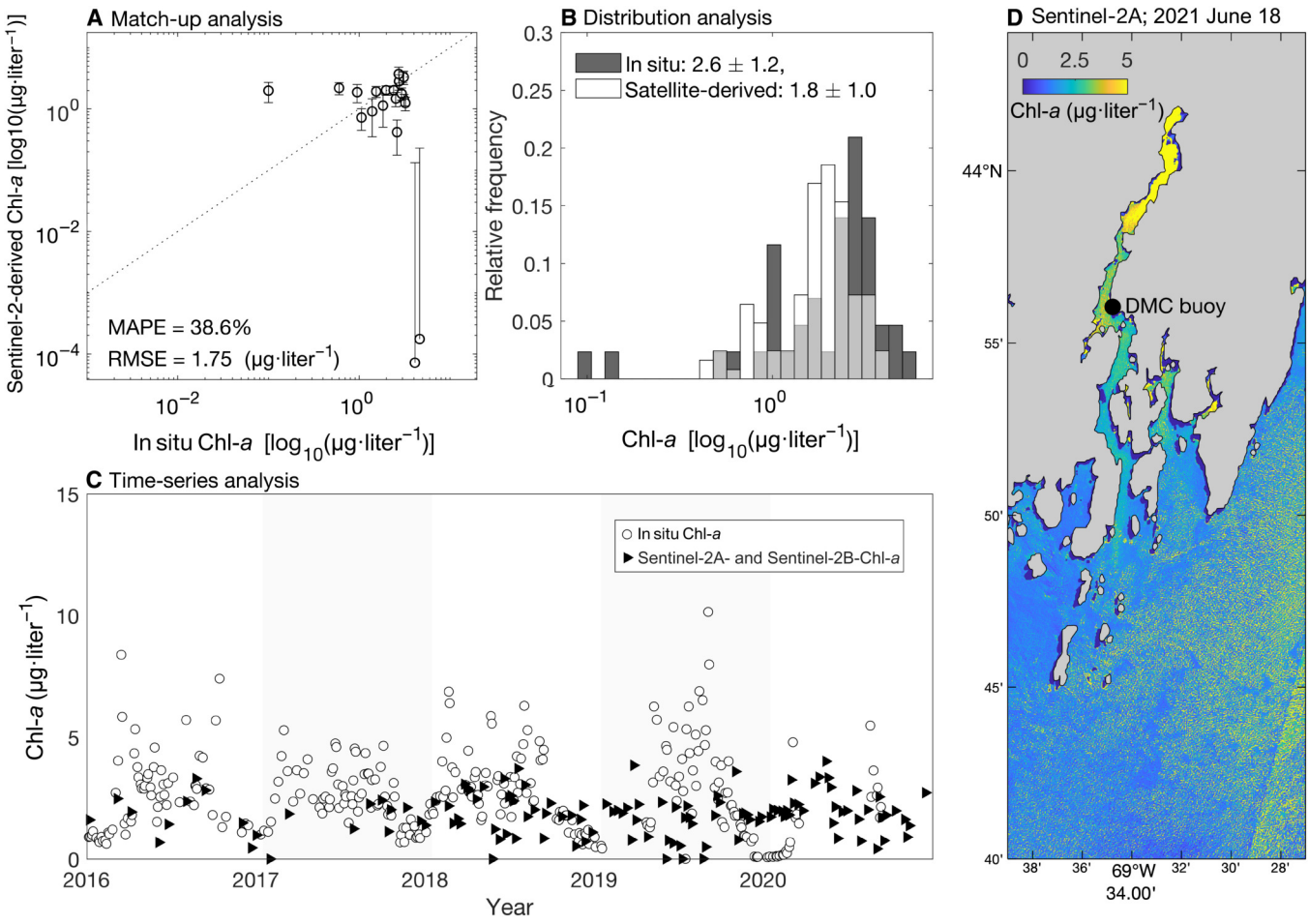

Fig. 6. Analysis of Chl-*a* in Damariscotta River Estuary from Sentinel-2A and Sentinel-2B. (A) depicts the match-up analysis between the daily in situ and Sentinel-2-derived Chl-*a*. Vertical bars represent the standard deviation of 7-by-7 pixels within each sampling box. (B) depicts the data distribution. (C) represents the time series from both in situ and Sentinel-2. (D) represents the high-resolution spatial distribution of Chl-*a* on 2021 June 18 (black dot represents the location of in situ data at the University of Maine's Darling Marine Center dock). MAPE, mean absolute percentage error; RMSE, root mean square error.

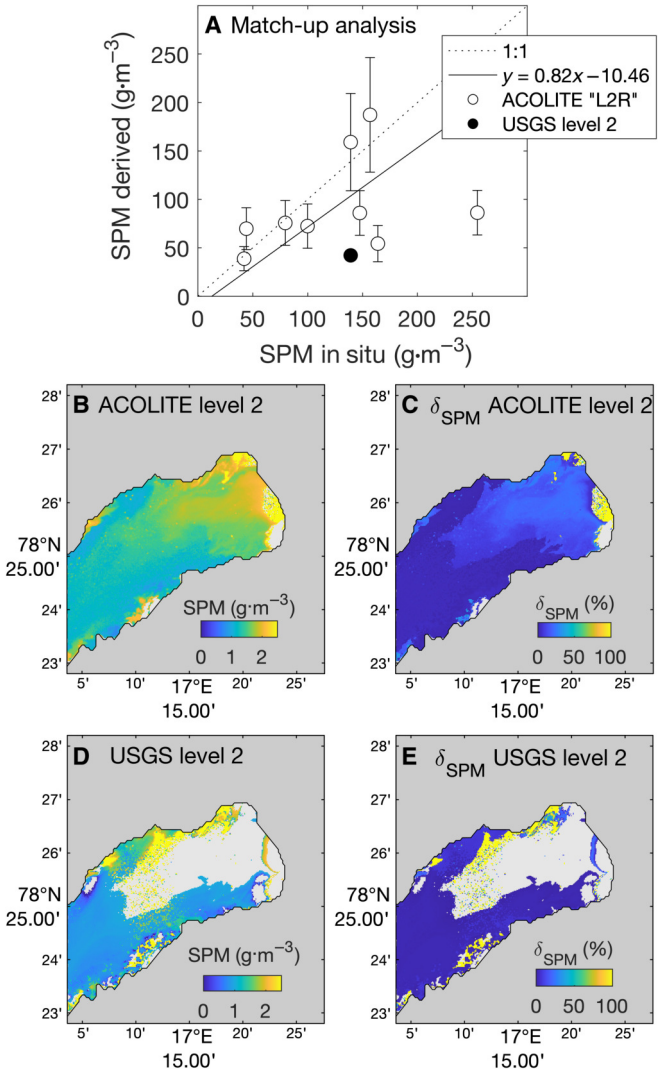

Fig. 7. Analysis of SPM in Tempelfjorden, Svalbard, Norway from the Landsat-8 sensor. (A) shows the match-up between in situ and satellite-derived SPM within the day of satellite overpass. SPM was derived from the use of 3 satellite bands: 655, 865, and 1,609 nm [52]. Vertical bars represent the derived uncertainties in SPM. The black dot in the plot represents one match-up available between in situ SPM and the SPM derived from USGS level 2. (B) represents the spatial distribution of SPM from level 2 R_{rs} acquired after ACOLITE processing. (C) depicts the uncertainties in SPM retrievals of (B). (D) represents SPM from the R_{rs} from the standard USGS algorithm. The light gray area is data masked from USGS QA file, and panel shows uncertainties for the SPM depicted in (D).

Except for lingering across track issues, this product fares well in both cross-calibration with other sensors and in situ validation with AERONET-OC [15]. More information about the product is available here (https://www.usgs.gov/landsat-missions/landsat-collection-2-provisional-aquatic-reflectance-science-product).

As an example, we present data for a complex region stretching from the extremely turbid and productive Pamlico–Albemarle estuary, North Carolina, USA into the oligotrophic Gulf Stream off Cape Hatteras, North Carolina and compare the aquatic reflectance product with the standard level 2 surface reflectance from Landsat-9 and the standard level 2 ocean color R_{rs} from MODIS-aqua (Fig. 4). The Landsat aquatic reflectance and surface reflectance products are divided by π to convert to R_{rs} for comparison with MODIS. The improved AC compared to the standard product is especially noticeable in the blue Gulf Stream waters. Much finer spatial detail is observable in the Chl-*a* product of the aquatic R_{rs} product compared to the standard R_{rs} as evidenced by the fine-scale eddy along the Gulf Stream front and the outflow from the inlet. The increase in spatial resolution over MODIS is especially striking around the inlets and capes of the coastline. As noted in validation studies [15], the blue reflectance computed for Landsat is higher than MODIS, and across-track discontinuities are apparent in both the aquatic and surface Landsat products and derived Chl-*a*. All code to process the Landsat aquatic reflectance product and example data to produce the imagery in Fig. 4 is available.

Coastal Maine Chl-*a*

For this case study on the coast of Maine (Sentinel-2; swath: 43 to 44 °N, 69.65 to 69.45 °W), we present 2 sets of results: a comparison of AC schemes (Fig. 5) and a time series of Sentinel-2A and Sentinel-2B (from 2016 to 2022), level 1C TOA scenes processed to level 2 using AC from POLYMER (Fig. 6).

We first compare reflectances obtained with 5 different AC software: SeaDAS (l2gen: aer opt -2), POLYMER (default), C2RCC (C2RCC-Nets), OCSMART (default), and ACOLITE [dark spectrum fitting added to 4 different regions of interest (roi; i.e., 100-by-100, 300-by-300, 600-by-600, and 1,200-by-1,200 pixels used to specify the dark spectrum)]. From these level 2 scenes, we extracted the median R_{rs} spectra for a 7-by-7-pixel area centered at an in situ sampling site [i.e., upper Damariscotta River Estuary (http://maine.loboviz.com/loboviz/)] and applied the QWIP algorithm for QC (Fig. 5) [48]. Note that all AC-corrected spectra with $|\text{QWIP}| \leq 0.2$ have similar red reflectance and hence will be in close agreement with respect to the SPM value.

Last, we statistically assessed Chl-*a* retrievals and observations that the AC scheme provided in POLYMER and the OCx algorithm for Chl-*a* matched observations best for this region (Fig. 6), consistent with [16].

Tempelfjorden, Svalbard SPM

For this case study, we use a series of in situ and remote sensing measurements collected during a 2015 campaign in a narrow glaciated fjord in Svalbard, Norway (Tempelfjorden) [58]. Here, we focus on the in situ surface SPM samples collected on the same day of the Landsat-8 overpass (14 August 2015). On this day, 11 in situ SPM samples were collected from a rigid inflatable boat both inside and outside the subglacial discharge plume (Fig. 7). Surface SPM water samples were collected in 1 liter of volumes and filtered using a Suction Buchner system with 45 mm, 47-µm cellulose filters. These SPM concentrations ranged from 42 to 347 $g \cdot m^{-3}$, providing a range of values to compare against 2 sources of satellite derived products. (a) Surface reflectance data from Landsat-8 R_{rs} collection 2 level 2 (recommended for land), using the standard USGS algorithm, were downloaded, and (b) a level 2 output ('$*$ *L2R*' file) derived from the ACOLITE dark spectrum scheme was used. Because USGS level 2 collection 2 bands are made available in an unsigned integer data format, a conversion to water reflectance is necessary http://www.pancroma.com/downloads/Using the USGS Landsat 8 Product.htm. Once transformed to R_{rs} level 2 data, we applied the multiwavelength algorithm [52] that provides both SPM values and associated uncertainties.

We depict the relationship between SPM from both sources of R_{rs} and from the in situ observations in Fig. 7. Although we

use only 11 in situ data points, it is enough to demonstrate how to (a) convert of unsigned integers from standard USGS products to R_{rs}, (b) compare of R_{rs} from multiple sources of level 2 scenes, and (b) illustrate the richness of information from spatial distribution of uncertainties. Last, we find the USGS Level 2 data to be masked over much of the scene, unlike that of ACOLITE.

Long-term turbidity estimates from Patos Lagoon Estuary, Brazil

For this case study, we collected cloud-free level 1 scenes from Landsat-5, Landsat-7, Landsat-8, and Landsat-9 sensors between 1984 and 2022 in the Patos Lagoon Estuary, Brazil (swath: 31.7 to 32.4 °S, 51.8 to 52.3 °W). The Landsat imagery covered the following time periods: 1984–2011 (Landsat-5), 1999–2003 (Landsat-7), 2013–2022 (Landsat-8), and 2021–2022 (Landsat-9). AC was carried out using the ACOLITE processor with default AC (i.e., dark spectrum) and ancillary data.

Next, to simplify the exercise, we use ACOLITE to derive turbidity with the [59] generic algorithm (in the NIR band to avoid R_{rs} saturation) available within the processor.

Level 2 satellite scenes (i.e., *.L2W files) are examined with MATLAB scripts (*.m; see the Supplementary Materials—Case 3.3) to generate a long time series of turbidity. Files are named by the order of steps (e.g., step01..., step02...) to make processing more intuitive. The step01* script finds match-ups between in situ sampled turbidity and satellite overpasses (at a given 5-by-5-pixel area), a maximum of 30-min time interval between the satellite overpass and in situ data, and latitude and longitude specified from the same in situ data (https://simcosta.furg.br/), based on the recommendations of the International Ocean Colour Coordinating Group [64] (Fig. 8A).

Match-up analysis is for the period between 2016 and 2021, when systematic in situ data sampling was available. With this match-up dataset, a regional calibration is applied to satellite-derived turbidity using a power-law regression. To obtain

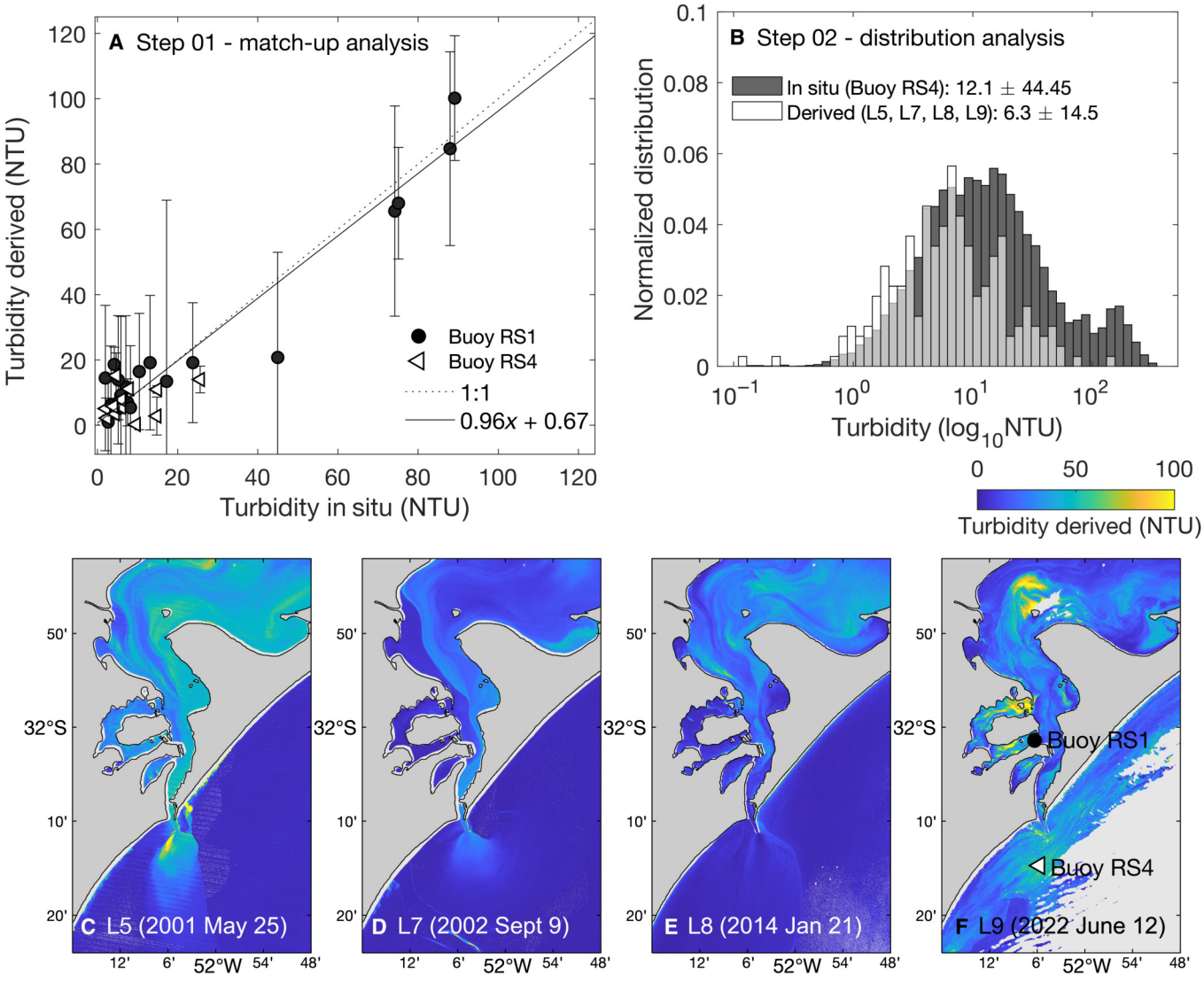

Fig. 8. Analysis of turbidity in Patos Lagoon Estuary, Brazil from Landsat-5, Landsat-7, Landsat-8, and Landsat-9 sensors. Two buoy stations were used to provide a comparison example between satellite-derived and in situ turbidity. (A) shows regionally calibrated match-ups between satellite derived and in situ turbidity for Buoys RS1 and RS4 within 30-min maximum interval and a 3-by-3-pixel window. Vertical bars represent the standard deviation of pixels within each sampling box. (B) represents the data distribution of in situ and satellite-derived turbidity sampled at station Buoy RS4. (C) to (F) depict one example of calibrated satellite-derived turbidity for each sensor. Location of in situ stations is depicted in (F).

locally calibrated turbidity, we applied a type II regression, along with a computation of Kendall's Tau correlation coefficient, root mean square deviation, and median absolute deviation. Because of lack of match-up data available for the time covered by Landsat-5 and Landsat-7, an additional approach, the turbidity distribution, for comparison between in situ measured and satellite data is available in the step02* script (Fig. 8B). Those steps are necessary to guarantee that satellite-derived turbidity is within an acceptable uncertainty compared to in situ measured turbidity data.

The step03* script plots a map of the turbidity satellite scene for each Landsat sensor using the "m_map" package (https://www.eoas.ubc.ca/~rich/map.html) (Fig. 8C to F).

Final Remarks

To date, the use of high-resolution water color and SST data has been mostly in the hands of expert users. In this paper, we attempt to push toward the democratization of these data so that a broader audience can use them. Our goal was to provide sufficient information so that users without specialized knowledge of remote sensing data and/or AC, particularly newcomers, can determine which steps are necessary for them to process water color products from the rich archive of high resolution open-access remote sensing data. We have found that this information was somewhat lacking and hope to thus save time for newcomers to this field. We emphasize that to establish confidence in the data retrieved and quantify uncertainty, in situ data are necessary. In essence, satellites are used to interpolate in time and space between in situ data, and this interpolation becomes tenuous without appropriate in situ data. While we mentioned several tools to QA/QC of the R_{rs} spectra, they are not sufficient to establish the quality of derived parameters. This is because changes in the nature of the underlying parameters (e.g., sediment mineralogy and phytoplankton species composition) can change their mass specific optical properties and, hence, their impact on the light leaving a water body. Last, we hope that the case studies presented here are useful and that new and old practitioners alike get in the habit of sharing their code and data together with their investigations, to the benefit of the whole community.

We have provided recipes here for the derivation of water quality products that we hope will be widely used. However, we urge national and international organizations to distribute such products to the public. Since substantial public funds have been used to fund these satellite missions, it is only reasonable to expect that such products be widely and freely available and not just the radiance from which they are derived.

Acknowledgments

This project came out of a winter class at UMaine proposed by B. Van Dam and focused on high-resolution remote sensing. Through the class, we discovered how nontrivial the process of deriving and validating water quality products is, motivating us to work on this primer. We would like to thank SIMCOSTA (https://simcosta.furg.br/), USGS, ESA, and NASA for the open policy data availability. We would like to thank E. Fernandes. J.T. thanks D. van der Wal for supervision and guidance and thanks University of Twente and ITC for support. We thank M. Peters support for C2RCC AC by SNAP, F. Steinmetz support for Polymer, Q. Vanhellemont support for ACOLITE, and Y. Fan support for OCSMART. **Funding:** We thank NASA for Future Investigators in NASA Earth and Space Science and Technology (FINESST) funding for P.G. (80NSSC19K1366) and G.B. (80NSSC20K1641) and funding for K.M.S. to conduct the Svalbard fieldwork (NNX10AG22G). We thank National Sea Grant NOAA Award NA18OAR4170330 for providing E.B., T.K., and D.C.B. support for aquaculture applications of high-resolution remote sensing products. Additional support for T.K. and D.C.B. came from USDA National Institute of Food and Agriculture (project number ME0-830-31000-004-00D). B.J. thanks the China Scholarship Council (no. CSC201906260052). **Author contributions:** Conceptualization and coordination were done by E.B. Methodology was done by J.T., B.J., T.K., G.B., P.G., L.S.d.C., G.H., K.M.S., and E.B. Software was done by J.T., B.J., T.K., G.B., L.S.d.C., P.G., G.H., and L.F.d.S. Resources were done by J.T., B.J., T.K., G.B., P.G., L.S.d.C., G.H., K.M.S., and E.B. Writing—original draft preparation was done by J.T., B.J., T.K., G.B., P.G., L.S.d.C., K.M.S., and E.B. Writing—review and editing was done by J.T., B.J., T.K., G.B., P.G., L.S.d.C., K.M.S., D.C.B., and E.B. All authors have read and agreed to the published version of the manuscript. **Competing interests:** The authors declare that they have no competing interests.

Data Availability

The data used in the case studies of this document are either available with from the link to the software of the case studies or is available within the same directories. Case studies and codes are available at https://github.com/OceanOptics/High-resolution-satellites-primer-codes

Supplementary Materials

Fig. S1. Location map of each case study presented and dataset(s) used.
Table S1. Summary of high-resolution satellite specifications.
Table S2. Spectral and radiometric resolutions of Landsat-5, Landsat-7, Landsat-8, and Landsat-9.
Table S3. Spectral and radiometric resolution of Sentinel-2A and Sentinel-2B.

References

1. Ekstrand S. Landsat TM based quantification of chlorophyll-a during algae blooms in coastal waters. *Int J Remote Sens*. 1992;13(10):1913–1926.
2. Torbick N, Hession S, Hagen S, Wiangwang N, Becker B, Qi J. Mapping inland lake water quality across the Lower Peninsula of Michigan using Landsat TM imagery. *Int J Remote Sens*. 2013;34(21):7607–7624.
3. Montanher OC, Novo EM, Barbosa CC, Rennó CD, Silva TS. Empirical models for estimating the suspended sediment concentration in Amazonian white water rivers using Landsat 5/TM. *Int J Appl Earth Obs Geoinf*. 2014;29:67–77.
4. Barnes BB, Hu C, Holekamp KL, Blonski S, Spiering BA, Palandro D. Use of Landsat data to track historical water quality changes in Florida keys marine environments. *Remote Sens Environ*. 2014;140:485–496.
5. Zhang M, Dong Q, Cui T, Xue C, Zhang S. Suspended sediment monitoring and assessment for Yellow River estuary from Landsat TM and ETM+ imagery. *Remote Sens Environ*. 2014;146:136–147.

6. Franz BA, Bailey SW, Kuring N, Werdell PJ. Ocean color measurements with the Operational Land Imager on Landsat-8: Implementation and evaluation in SeaDAS. *J Appl Remote Sens*. 2015;9(1):096070.
7. Snyder J, Boss E, Weatherbee R, Thomas AC, Brady D, Newell C. Oyster aquaculture site selection using Landsat 8-derived sea surface temperature, turbidity, and chlorophyll *a*. *Front Mar Sci*. 2017;4:190.
8. Gernez P, Doxaran D, Barillé L. Shellfish aquaculture from space: Potential of sentinel2 to monitor tide-driven changes in turbidity, chlorophyll concentration and oyster physiological response at the scale of an oyster farm. *Front Mar Sci*. 2017;4:137.
9. Vanhellemont Q, Ruddick K. Turbid wakes associated with offshore wind turbines observed with Landsat 8. *Remote Sens Environ*. 2014;145:105–115.
10. Trinh R, Fichot C, Gierach M, Holt B, Malakar N, Hulley G, Smith J. Application of Landsat 8 for monitoring impacts of wastewater discharge on coastal water quality. *Front Mar Sci*. 2017;4:329.
11. Niroumand-Jadidi M, Bovolo F, Bresciani M, Gege P, Giardino C. Water quality retrieval from landsat-9 (oli-2) imagery and comparison to sentinel-2. *Remote Sens*. 2022;14(18):4596.
12. Mobley CD, Werdell J, Franz B, Ahmad Z, Bailey SW. Atmospheric correction for satellite ocean color radiometry. No. GSFC-E-DAA-TN35509; 2016 June 1.
13. Werdell PJ, McKinna LI, Boss E, Ackleson SG, Craig SE, Gregg WW, Lee Z, Maritorena S, Roesler CS, Rousseaux CS, et al. An overview of approaches and challenges for retrieving marine inherent optical properties from ocean color remote sensing. *Prog Oceanogr*. 2018;160:186–212.
14. Begouen Demeaux C, Boss E. Validation of remote-sensing algorithms for diffuse attenu- ation of downward irradiance using BGC-Argo floats. *Remote Sens*. 2022;14(18):4500.
15. Pahlevan N, Schott JR, Franz BA, Zibordi G, Markham B, Bailey S, Schaaf CB, Ondrusek M, Greb S, Strait CM. Landsat 8 remote sensing reflectance (R_{rs}) products: Evaluations, intercomparisons, and enhancements. *Remote Sens Environ*. 2017;190:289–301.
16. Jiang B, Boss E, Kiffney T, Hesketh G, Bourdin G, Fan D, Brady DC. Oyster aquaculture site selection using high-resolution remote sensing: A case study in the Gulf of Maine, United States. *Front Mar Sci*. 2022;9:802438.
17. Frouin RJ, Franz BA, Ibrahim A, Knobelspiesse K, Ahmad Z, Cairns B, Chowdhary J, Dierssen HM, Tan J, Dubovik O, et al. Atmospheric correction of satellite ocean-color imagery during the PACE Era. *Front Earth Sci*. 2019;7: 10.3389/feart.2019.00145.
18. Moses WJ, Sterckx S, Montes MJ, De Keukelaere L, Knaeps E. Chapter 3 - atmospheric correction for inland waters. In: Mishra DR, Ogashawara I, Gitelson AA, eds. *Bio-optical modeling and remote sensing of inland waters*, Elsevier; 2017. p. 69–100.
19. Pahlevan N, Mangin A, Balasubramanian SV, Smith B, Alikas K, Arai K, Barbosa C, Bélanger S, Binding C, Bresciani M, et al. Acix-aqua: A global assessment of atmospheric correction methods for Landsat-8 and Sentinel-2 over lakes, rivers, and coastal waters. *Remote Sens Environ*. 2021;258:112366.
20. Santos DRAe, Martinez JM, Harmel T, Borges HD, Roig H, Evaluation of sentinel-2/Msi imagery products level-2a obtained by three different atmospheric corrections for monitoring suspended sediments concentration in Madeira River, Brazil. Paper presented at: Proceedings of the 2020 IEEE Latin American GRSS & ISPRS Remote Sensing Conference (LAGIRS); 2020 March 22–26; Santiago, Chile.
21. Martins VS, Barbosa CCF, De Carvalho LAS, Jorge Fereira DS, De Lucia Lobo F, Leão de Moraes Novo EM. Assessment of atmospheric correction methods for sentinel-2 MSI images applied to amazon floodplain lakes. *Remote Sens*. 2017;9(4):322.
22. Bui Q-T, Jamet C, Vantrepotte V, Mériaux X, Cauvin A, Mograne MA. Evaluation of sentinel-2/MSI atmospheric correction algorithms over two contrasted French coastal waters. *Remote Sens*. 2022;14(5):1099.
23. Warren M, Simis S, Martinez-Vicente V, Poser K, Bresciani M, Alikas K, Spyrakos E, Giardino C, Ansper A. Assessment of atmospheric correction algorithms for the Sentinel-2a MultiSpectral Imager over coastal and inland waters. *Remote Sens Environ*. 2019;225:267–289.
24. Vanhellemont Q. Adaptation of the dark spectrum fitting atmospheric correction for aquatic applications of the Landsat and Sentinel-2 archives. *Remote Sens Environ*. 2019;225:175–192.
25. Vanhellemont Q, Ruddick K. Advantages of high quality SWIR bands for ocean colour processing: Examples from Landsat-8. *Remote Sens Environ*. 2015;161:89–106.
26. Vanhellemont Q, Ruddick K, Acolite for Sentinel-2: Aquatic applications of MSI imagery. Paper presented at: Proceedings of the 2016 ESA Living Planet Symposium; 2016 May 9–13; Prague, Czech Republic.
27. Fan Y, Li W, Chen N, Ahn J-H, Park Y-J, Kratzer S, Schroeder T, Ishizaka J, Chang R, Stamnes K. OC-SMART: A machine learning based data analysis platform for satellite ocean color sensors. *Remote Sens Environ*. 2021;253:112236.
28. Steinmetz F, Deschamps P-Y, Ramon D. Atmospheric correction in presence of sun glint: Application to MERIS. *Opt Express*. 2011;19(10):9783–9800.
29. Brockmann C, Doerffer R, Peters M, Kerstin S, Embacher S, Ruescas A. Evolution of the C2RCC neural network for sentinel 2 and 3 for the retrieval of ocean colour products in normal and extreme optically complex waters. 2016;740:54.
30. Fan Y, Li W, Gatebe C, Jamet C, Zibordi G, Schroeder T, Stamnes K. Atmospheric correction over coastal waters using multilayer neural networks. *Remote Sens Environ*. 2017;199:218–240.
31. Gordon HR, Wang M. Influence of oceanic whitecaps on atmospheric correction of ocean-color sensor. *Appl Opt*. 1994;33:7754–7763.
32. Bulgarelli B, Zibordi G. On the detectability of adjacency effects in ocean color remote sensing of mid-latitude coastal environments by SeaWiFS, MODIS-A, MERIS, OLCI, OLI and MSI. *Remote Sens Environ*. 2018;209:423–438.
33. Ansper A, Alikas K. Retrieval of chlorophyll *a* from Sentinel-2 MSI data for the European Union water framework directive reporting purposes. *Remote Sens*. 2019;11(1):64.
34. Paulino RS, Martins VS, Novo EMLM, Barbosa CCF, de Carvalho LAS, Begliomini FN. Assessment of adjacency correction over inland waters using sentinel-2 MSI images. *Remote Sens*. 2022;14(8):1829.
35. Steinmetz F, Ramon D. Sentinel-2 MSI and sentinel-3 OLCI consistent ocean colour products using polymer. In: *Remote sensing of the open and coastal ocean and inland waters*. Honolulu (HI): SPIE; 2018. pp. 46–55.
36. Bouali M, Ladjal S. Toward optimal destriping of MODIS data using a unidirectional variational model. *IEEE Trans Geosci Remote Sens*. 2011;49(8):2924–2935.

37. Mills S, Miller S. VIIRS day/night band—Correcting striping and nonuniformity over a very large dynamic range. *J Imaging*. 2016;2(1):9.
38. Pahlevan N, Lee Z, Wei J, Schaaf CB, Schott JR, Berk A. On-orbit radiometric characterization of OLI (Landsat-8) for applications in aquatic remote sensing. *Remote Sens Environ*. 2014;154:272–284.
39. Gascon F, Bouzinac C, Thépaut O, Jung M, Francesconi B, Louis J, Lonjou V, Lafrance B, Massera S, Gaudel-Vacaresse A, et al. Copernicus Sentinel-2A calibration and products validation status. *Remote Sens*. 2017;9(6):584.
40. Wang M, Hu C. Automatic extraction of *Sargassum* features from Sentinel-2 MSI images. *IEEE Trans Geosci Remote Sens*. 2021;59(3):2579–2597.
41. Coffer MM, Whitman PJ, Schaeffer BA, Hill V, Zimmerman RC, Salls WB, Lebrasse MC, Graybill DD. Vertical artifacts in high-resolution WorldView-2 and WorldView-3 satellite imagery of aquatic systems. *Int J Remote Sens*. 2022;43(4):1199–1225.
42. Rasti B, Chang Y, Dalsasso E, Denis L, Ghamisi P. Image restoration for remote sensing: Overview and toolbox. *IEEE Geosci Remote Sens Mag*. 2022;10(2):201–230.
43. Bouali M, Ignatov A. Adaptive reduction of striping for improved sea surface temperature imagery from Suomi National Polar-Orbiting Partnership (S-NPP) Visible Infrared Imaging Radiometer Suite (VIIRS). *J Atmos Ocean Technol*. 2014;31(1):150–163.
44. Banerjee S, Shanmugam P. An improved method for destriping of VIIRS day/night band images. *IEEE Access*. 2022;10:82164–82184.
45. Liu JG, Morgan GLK. FFT Selective and adaptive filtering for removal of systematic noise in ETM+ imageodesy images. *IEEE Trans Geosci Remote Sens*. 2006;44(12):3716–3724.
46. Wang J-L, Huang T-Z, Ma T-H, Zhao X-L, Chen Y. A sheared low-rank model for oblique stripe removal. *Appl Math Comput*. 2019;360:167–180.
47. Wei J, Lee Z, Shang S. A system to measure the data quality of spectral remote-sensing reflectance of aquatic environments. *J Geophys Res Oceans*. 2016;121(11):8189–8207.
48. Dierssen HM, Vandermeulen RA, Barnes BB, Castagna A, Knaeps E, Vanhellemont Q. QWIP: A quantitative metric for quality control of aquatic reflectance spectral shape using the apparent visible wavelength. *Front Remote Sens*. 2022;3:869611.
49. Vandermeulen RA, Mannino A, Craig SE, Werdell PJ. 150 shades of green: Using the full spectrum of remote sensing reflectance to elucidate color shifts in the ocean. *Remote Sens Environ*. 2020;247:111900.
50. Luo Y, Doxaran D, Ruddick K, Shen F, Gentili B, Yan L, Huang H. Saturation of water reflectance in extremely turbid media based on field measurements, satellite data and bio-optical modelling. *Opt Express*. 2018;26(8):10435.
51. Novoa S, Doxaran D, Ody A, Vanhellemont Q, Lafon V, Lubac B, Gernez P. Atmospheric corrections and multi-conditional algorithm for multi-sensor remote sensing of suspended particulate matter in low-to-high turbidity levels coastal waters. *Remote Sens*. 2017;9(1):61.
52. Tavora J, Boss E, Doxaran D, Hill P. An algorithm to estimate suspended particulate matter concentrations and associated uncertainties from remote sensing reflectance in coastal environments. *Remote Sens*. 2020;12(13):2172.
53. Pahlevan N, Smith B, Alikas K, Anstee J, Barbosa C, Binding C, Bresciani M, Cremella B, Giardino C, Gurlin D, et al. Simultaneous retrieval of selected optical water quality indicators from Landsat-8, Sentinel-2, and Sentinel-3. *Remote Sens Environ*. 2022;270:112860.
54. Wei J, Lee ZP, Shang S, Yu X. Semianalytical derivation of phytoplankton, CDOM, and detritus absorption coefficients From the Landsat 8/OLI reflectance in coastal waters. *J Geophys Res Oceans*. 2019;124(6):3682–3699.
55. Lee ZP. Applying narrowband remote-sensing reflectance models to wideband data. *Appl Opt*. 2009;48(17):3177–3183.
56. Burggraaff O. Biases from incorrect reflectance convolution. *Opt Express*. 2020;28(9):13801.
57. Nechad B, Ruddick KG, Park Y. Calibration and validation of a generic multisensor algorithm for mapping of total suspended matter in turbid waters. *Remote Sens Environ*. 2010;114(4):854–866.
58. Schild KM, Hawley RL, Chipman JW, Benn DI. Quantifying suspended sediment concentration in subglacial sediment plumes discharging from two Svalbard tidewater glaciers using Landsat-8 and in situ measurements. *Int J Remote Sens*. 2017;38(23):6865–6881.
59. Nechad B, Ruddick KG, Neukermans G. Calibration and validation of a generic multisensor algorithm for mapping of turbidity in coastal waters. In: *Remote sensing of the ocean, sea ice, and large water regions 2009*; SPIE; 2009. pp. 161–171.
60. Tavora J, Salama MS, Penning de Vries M, Mannaerts CM, van der Wal D, Detecting the effects of extreme events on estuarine suspended particulate matter using satellite remote sensing (Scheldt Estuary): Challenges and opportunities. *Remote Sens*. 2023;15(3):670.
61. Campbell JW. The lognormal distribution as a model for bio-optical variability in the sea. *J Geophys Res*. 1995;100(C7):13237.
62. Brewin RJW, Dall'Olmo G, Pardo S, van Dongen-Vogels V, Boss ES. Underway spectrophotometry along the Atlantic Meridional Transect reveals high performance in satellite chlorophyll retrievals. *Remote Sens Environ*. 2016;183:82–97.
63. Laws EA. *Mathematical methods for oceanographers: An introduction*. New York: Wiley-Interscience; 1997.
64. **IOCCG**. *Uncertainties in ocean colour remote sensing*. Mélin F, editor. Dartmouth, Canada: International Ocean Color Coordinating Group, 2019; http://dx.doi.org/10.25607/OBP-696.
65. Bailey S, Werdell PJ. A multi-sensor approach for the on-orbit validation of ocean color satellite data products. *Remote Sens Environ*. 2006;102(1–2): 12–23.
66. Boss E, Taylor L, Gilbert S, Gundersen K, Hawley N, Janzen C, Johengen T, Purcell H, Robertson C, Schar DWH, et al. Comparison of inherent optical properties as a surrogate for particulate matter concentration in coastal waters. *Limnol Oceanogr Methods*. 2009;7(11):803–810.
67. Neukermans G, Ruddick K, Loisel H, Roose P. Optimization and quality control of suspended particulate matter concentration measurement using turbidity measurements. *Limnol Oceanogr Methods*. 2012;10:1011–1023.
68. Gorelick N, Hancher M, Dixon M, Ilyushchenko S, Thau D, Moore R. Google Earth Engine: Planetary-scale geospatial analysis for everyone. *Remote Sens Environ*. 2017;202:18–27.
69. Ngoc DD, Loisel H, Jamet C, Vantrepotte V, Duforˆet-Gaurier L, Minh CD, Mangin A. Coastal and inland water pixels extraction algorithm (WiPE) from spectral shape analysis and HSV transformation applied to

Landsat 8 OLI and Sentinel-2 MSI. *Remote Sens Environ*. 2019;223:208–228.
70. Mabit R, Araújo CAS, Singh RK, Bélanger S. Empirical remote sensing algorithms to retrieve SPM and CDOM in Québec Coastal Waters. *Front Remote Sens*. 2022;3:834908.
71. Han B, Loisel H, Vantrepotte V, Mériaux X, Bryére P, Ouillon S, Dessailly D, Xing Q, Zhu J. Development of a semi-analytical algorithm for the retrieval of suspended particulate matter from remote sensing over clear to very turbid waters. *Remote Sens*. 2016;8(3):211.
72. Salama MS, Verhoef W. Two-stream remote sensing model for water quality mapping: 2SeaColor. *Remote Sens Environ*. 2015;157:111–122.
73. Arabi B, Salama MS, Pitarch J, Verhoef W. Integration of in-situ and multi-sensor satellite observations for long-term water quality monitoring in coastal areas. *Remote Sens Environ*. 2020;239:111632.
74. O'Reilly JE, Werdell PJ. Chlorophyll algorithms for ocean color sensors - OC4, OC5 & OC6. *Remote Sens Environ*. 2019;229:32–47.